

Temperature, Abundance, and Mass Density Profiling of the Perseus Galaxy Cluster

Paul Geringer

October 5, 2012

Abstract

Clusters of galaxies are massive structures containing approximately 10^{15} solar masses. The mass contained in clusters provided the first hints of the existence of dark matter. The hot intra-cluster medium (ICM), which is a gas with a temperature of 10^8 Kelvin, is easily detected by X-Ray telescopes. Of particular interest is the close Perseus galaxy cluster, one of the brightest X-Ray emitting galaxy clusters in the sky. Due to the large angular extent of the cluster, background noise subtraction is particularly challenging, and has yet to be completed using the full set of Perseus observations from the XMM-Newton X-Ray Telescope. Detailed temperature and abundance radial profile maps have revealed a significant lack of homogeneity within the cluster. Previous surveys of Perseus with the Suzaku telescope, which has a worse angular resolution and less light collecting area than XMM-Newton, revealed over-densities of X-Ray emission. These results provide evidence that the baryon fraction exceeds the universal average, which we had initially hoped to study. We have yet to confirm or deny the existence of clumping in these regions, which could explain such over-abundance of X-Ray emission.

This project offers a framework of efficient, automated processing techniques to “clean” images of noise from the mechanics of the telescope, background radiation from local sources such as the solar wind, and more distant sources such as background AGN. The galaxy cluster studied in this project contains high levels of contamination due to its line-of-sight position close to the dust- and star-filled arms of the Milky Way galaxy. Rigorous spectral model fitting of the cluster employ multiple parameters dedicated to accounting for these contaminations. The framework created from this analysis technique will provide the opportunity to expand this analysis to any nearby galaxy cluster, such as the Virgo, Coma, and Ophiuchus Clusters. This research should provide significant insight into how matter, both baryonic and dark matter, is distributed throughout diffuse cluster systems, as well as give clues to the origin of the ICM.

Contents

1	Introduction	3
1.1	Galaxy Clusters	3
1.2	Cluster Composition	3
1.3	Mass Determination	4
1.4	Motivation for Study	4
1.5	Expected Issues	5
2	Methodology	5
2.1	Initial Data Reduction	5
2.2	Masking and CCD Examination	6
2.3	Annulus Generation	7
2.3.1	Annulus Section Selection Algorithms	8
2.4	Objective and Background Spectra Generation	10
2.5	Automation Framework	11
2.6	Spectra Analysis	12
2.6.1	Spectra Preparation	12
2.6.2	Fitting Procedures	12
2.6.3	Soft Proton, Cosmic Background, and Instrumental effects	12
2.6.4	APEC and VAPEC Cluster Emission fitting	13
2.6.5	Mixing Model Fitting	13
3	Results	14
3.1	Tabulating Results	14
3.2	Calculation	14
3.3	Error Considerations	17
4	Future Study	19
5	Acknowledgements	20

1 Introduction

1.1 Galaxy Clusters

The study of X-Ray images of galaxy clusters is a relatively new field of astrophysical study that has benefitted greatly in the past decade from the launch of space based X-Ray observatories. Galaxy clusters are large, gravitationally bound systems consisting of many galaxies. The study of the physical characteristics of galaxy clusters offers key insight into cosmological parameters, such as the distribution of dark matter in the universe, the effects of the cosmological constant, and the distribution of baryonic matter in these enormous structures. Clusters often contain a central active galactic nuclei (AGN), which is theoretically powered by a matter-accreting supermassive black hole. Clusters themselves can be active as well; recently having experienced a collision with another cluster or adding a new component galaxy could be a potential cause for the cluster ICM to not be in hydrostatic equilibrium. Clusters that are in a relaxed hydrostatic equilibrium (1) state are typically modeled as spherically symmetric systems.

$$\frac{d\rho}{dr} = -\rho_g(r) \frac{GM(r)}{r^2} \quad (1)$$

Clusters offer numerous potential avenues of study. Clusters are used as model laboratories for investigating large scale creation and evolution of elements, as the large amounts of interacting gas are theorized to originate from stellar fusion processes. The extremely thin quantity of hot gas ($< 10^{-3}$ particles/cm $^{-3}$) in the ICM has emissions well within the X-Ray wavelength range. The composition and exact origin of this gas is an active area of research, which this study aims to explore in depth.

1.2 Cluster Composition

The main elemental composition of the ICM is important for a variety of reasons. The exact abundance of specific elements, such as iron, provides researchers with the ability to model the age and necessary mass of progenitor stars. Iron, which is produced as the upper fusion limit in high-mass stellar cores, can also be produced by the violent explosion of white dwarf stars in Type Ia supernovae. Mergers of the cluster with new component galaxies infuse the colliding ICM with high levels of supernova ejecta. By measuring the distribution of iron abundances, insight can be made into the evolutionary past of the star forming regions of the component galaxies of the cluster [2]. Similarly, alpha element abundances, which consist of O, Mg, Si, S, Ca and Ti, are of great importance to the study of the origin of the first stars and supernova. Following the more recent evolutionary track and formation of elements provides a more complete picture into how the current elemental composition of the universe came to be [3]. Recent studies have indicated that the majority of the iron abundance observed is directly formed in Type II supernovae, models of which are used to provide constraints on the rate of present and past star formation. This places limits on the timescale during which the iron and alpha element enrichment could have occurred [8].

1.3 Mass Determination

A frequently used technique in mass determinations is to assume the ICM of the cluster in question exhibits hydrostatic equilibrium as well as spherical symmetry. Using the model of hydrostatic equilibrium, one can derive a homogenous fit of gravitating mass across the observed portions of the cluster [11]. Such mass determinations have previously been emission model-dependent, relying upon multiple *a priori* assumptions concerning the state of the cluster beyond the aforementioned hypothesis of hydrostatic equilibrium and spherical symmetry. Recent advancements have been made to eliminate some of the *a priori* assumptions made in the case of mass determinations. In particular, the Navarro, Frenk, and White mass density model revealed that the density of dark matter halos around galaxy clusters, which form during the relaxation stage following mergers and collisions, do not necessarily depend on cosmological constants (Λ and Ω_m) or the power spectrum fit applied to the dark matter halo [9]. In recent years, even more significant advancements have been made, culminating in the development of cluster mass mixing models for X-Ray observations. In particular, the CLMASS and NFWMASS models provide a robust method of producing density and gravitational potentials for the spherical shells of clusters in hydrostatic equilibrium. In particular, when high quality observational data is available, these models provide significant improvements over the classical approach to mass determination [10].

1.4 Motivation for Study

This study concerns the analysis of archival data from the Perseus galaxy cluster. In a recent study by Simionescu et al., Suzaku data were used in conjunction with the CLMASS and NFWMASS models. The results from these fits reveal that the baryon gas fraction of the outer regions of the cluster (exceeding 2/3 of the virial radius) exceeds the cosmic average baryon gas fraction [13]. Such a result conflicts with accepted theory and provided additional motivation for this study of the Perseus Cluster.

The archival data obtained for this study is from the XMM-Newton telescope. This telescope, in comparison to Suzaku, offers significantly better angular resolution due to XMM-Newton's better optics. Suzaku had two main benefits, a shorter focal length and a lower radiation environment. These advantages give Suzaku a lower background emission profile. Suzaku also has a smaller light collecting area compared to XMM. With a higher angular resolution, evidence of clumping will become significantly more apparent when applying mass determination and density models to derived spectra. The larger effective light collecting area also provides the benefit of higher photon counts over a shorter exposure length, providing better overall statistics. This should offer the capability to detect any clumping of matter in regions noted to have higher-than-anticipated baryon gas fraction. If such clumping effects are observed, this could easily explain the conflict present in the Simionescu et al. study. Through this study, it is the goal of the investigator to supply ample reason for the continued study of diffuse and extended galaxy clusters using the analysis procedures to follow.

1.5 Expected Issues

The study of Perseus using the XMM-Newton observatory poses several unique problems. The field of view of the instrumentation on board the telescope is roughly $30'$. The cluster itself has an extent of nearly 2° , much larger than the FOV of the telescope. Because of the extent of the cluster, there is no region that can easily be selected to adequately model the background emission of the cluster. This issue is dealt with through the use of the ESAS data reduction package. This recently released analysis package provides several new tools to deal with background effects from extended diffuse X-Ray sources. This involves multiple tools designed particularly for the purpose of cleaning processed event files of soft proton, quiescent particle background, solar wind background, and crosstalk contamination (due to bright X-Ray sources located off-axis from the central observation heading). Furthermore, the novel use of ROSAT All-Sky Survey data as a spectral model to diffuse X-Ray background provides a powerful method to eliminate background emissions. Due to the very recent release of both the CLMASS and ESAS packages, this method of analysis has yet to be attempted on the Perseus galaxy cluster.

2 Methodology

2.1 Initial Data Reduction

The data processing techniques used to create spectra and images of the cluster are based off of the XMM-Newton Extended Source Analysis Software (ESAS) [14]. Significant improvements were made to the workflow of this software distribution. In particular, a fully automated framework was designed, based on work done in [16], to streamline data processing. Mechanisms to catch and eliminate errors were also introduced. This is discussed in more detail in §2.5.

The ESAS software package first examines and produces a set of unprocessed and uncleaned images directly from the detector with the `odfingest` routine. This is followed by the production of calibration files by the `cifbuild` routine, which allows reference calibration detector files to be used in the production of cluster and background spectra as well as image files.

A basic preparation task, `emchain`, first generates the event lists. Then, `mosfilter` (another utility), examines the unprocessed files for signs of obvious soft-proton contamination. It also provides a master clean file that is used to derive spectra. The soft-proton contamination characteristics can be examined directly through the plotting of the observation histogram and light curves (see Fig. 1). Observations that contain low levels of soft-proton events tend to have a light curve distribution that is generally uniform. Observations that do experience significant soft-proton contamination tend to observe low levels of high intensity events. Such contaminated observations in this study were noted, as further spectra fitting would indicate whether the not reliable results could be produced, or if the observation under study had to be discarded.

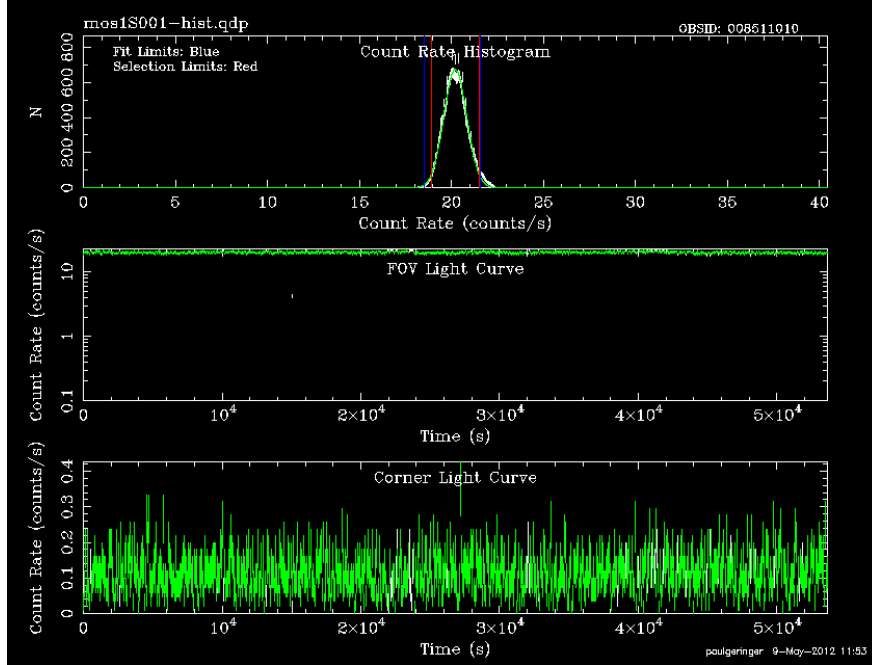


Figure 1: Light curves of the MOS1 detector for the first exposure of ObsID 0085110101.

2.2 Masking and CCD Examination

The first step to producing spectra involved the creation of point source mapping. As the primary processing techniques emphasized in ESAS are for diffuse spectra, point sources can cause a significant level of contamination in the resulting spectra. The ESAS **cheese** task was used to exclude such sources. The **cheese** utility runs source-detection algorithms to locate point sources, which are then added to a point source list. From this list, image masks (see Fig. 2) are created to exclude these point sources from final images.

Point sources were defined by the parameter selection of **cheese**. The threshold intensity value of an 10^{-14} ergs/s cm² was used for the detection of potential point sources. Detected sources were then excised by removing the region radially surrounding the source to half the surface brightness of the background. The source detection algorithm was limited so that sources within 40'' of each other were not excluded, so as to prevent brighter, extended sources from excision. However, this required the manual examination of the image for bright, closely-packed foreground sources, which the **cheese** task would skip. Any such sources were then excluded.

For the purpose of this study, images were generated by **cheese** and all subsequent tasks. Masks generated by **cheese** were made for the range of energies between 400 eV through 10 keV.

Detector images of the observation were then examined for CCDs operating in anomalous states. CCDs behaving in this format tend to over-estimate low energy (< 1 keV) background. As the Perseus cluster has significant low energy emission (~ 0.3 keV), exclusion of anomalous CCDs states was vital. CCDs were determined to be in anomalous states through the output of the corner hardness ratios in the **mos-filter** task as well as

examining the images visually. A shell script was used to extract the notably bad CCDs from the output of `mos-filter` and automatically set future tasks to exclude them from processing.

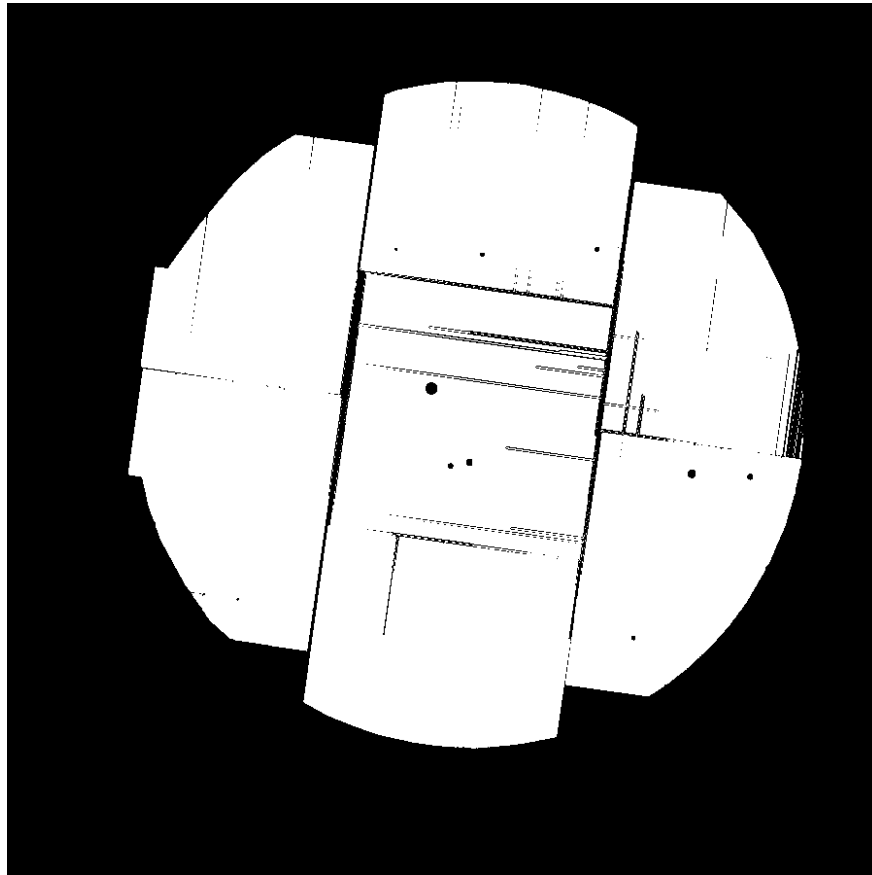


Figure 2: Cheese mask image of ObsID 0085110101. This image indicates the overall profile of the MOS detectors.

2.3 Annulus Generation

Production of the annular shaped sections was necessary for **CLMASS** and **NFWMASS** mixing model analysis. This required the creation of several Python-based programs to create spectra across identical sky coordinates for both MOS detectors. Instead of creating masking regions for the included `mos-spectra` and `mos_back` tasks, partial annuli of events were computed directly from event files. This involved use of the `kapteyn` Python module and a novel rotation algorithm described below. An example of the resulting event files can be seen in Fig. 3. When generating an annular section, the events contained by the annulus section were rewritten into a new event file containing the identical FITS formatted header of the original event file.

This program can be run in two modes, generating events of full cluster annuli or annuli sections propagating in a specific radial direction from the cluster center. This system

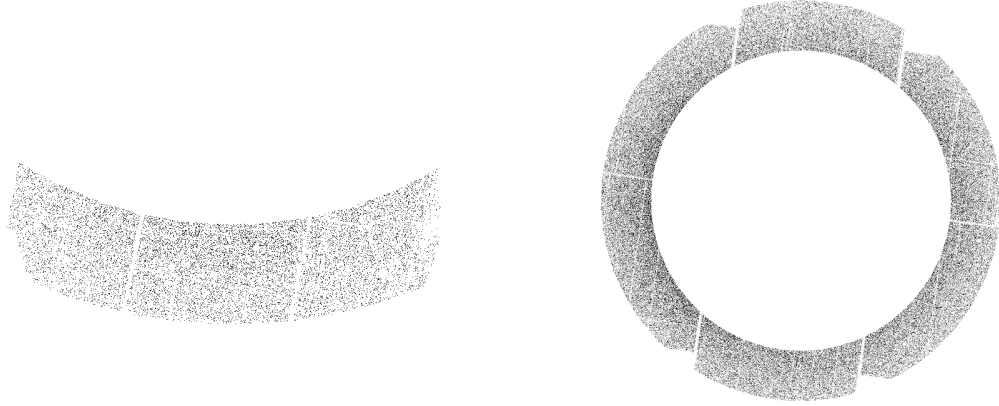


Figure 3: Left: A partial annulus from a non-center observation. Right: A full annulus from the center cluster observation.

permits a wide variety of potential analysis and lends itself particularly well to the use of spectra in mass mixing models (such as **CLMASS** and **NFWMASS**), which determine the characteristics of the spherical shells defined by the cylinder of three-dimensional emission described by the annuli (Fig. 4).

Event files that were generated were sorted according to the radial spacing between the great arcs describing the annulus as well as the angle in radians described by the flat edges of the annulus. This is particularly useful when generating spectra of the full annulus encompassing the cluster, as it determines the exact angular extent of each annulus. In the case of directional analysis, this is particularly beneficial for any situation where a direction chosen might lie along the edge of the observations field of view; the angle is defined by the maximum and minimum right ascension of all events within the reformatted event file. This angle generation is vital for the use of many mixing models, as it is necessary to describe the particular region over which to apply the model.

2.3.1 Annulus Section Selection Algorithms

Two annulus selection algorithms were used in this research:

- *partialAnnulus*: Used to compute an annulus section \mathcal{S} given an inner radius r_1 , an outer radius r_2 , and two bounding angles θ_1 and θ_2 .
- *fullAnnulus*: Used to compute an annulus \mathcal{A} given by radii r_1 and r_2 , along with an associated bounding angles in the case that the annulus was not complete (i.e. when the annulus was generated from a peripheral, non-center observation).

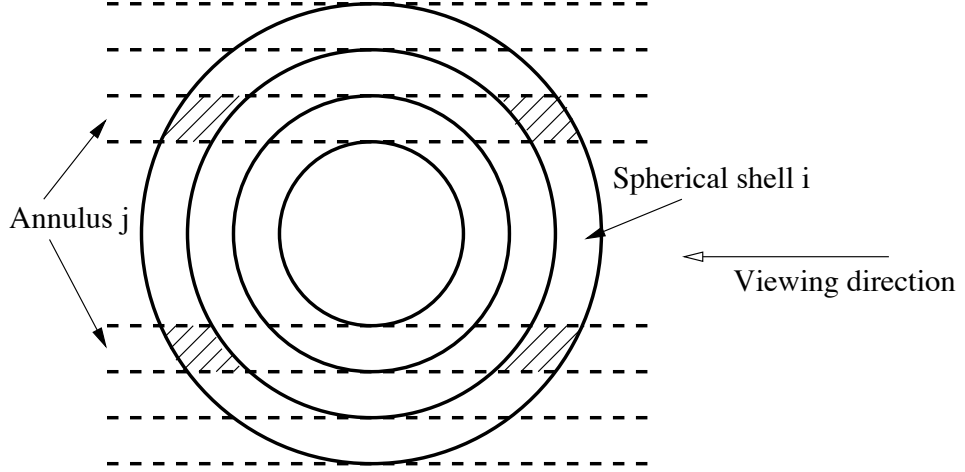


Figure 4: Diagram of spherical shells of cluster from [10].

```

partialAnnulus(evtfile,  $\rho_0, \delta_0, r_1, r_2, \theta_1, \theta_2$ ):
    rotevts  $\leftarrow$  map rot( $\rho_0, \delta_0, \cdot, \cdot$ ) on evtfile
    return  $\{\rho', \delta' \in \text{rotevts} : \theta_1 \leq \rho' \leq \theta_2 \ \& \ r_1 \leq \delta' \leq r_2\}$ 

```

Table 1: A *pseudo-code* implementation of the *partialAnnuli* routine in mathematical shorthand.

```

fullAnnulus(evtfile,  $\rho_0, \delta_0, r_1, r_2$ ):
    rotevts  $\leftarrow$  map rot( $\rho_0, \delta_0, \cdot, \cdot$ ) on evtfile
     $\mathcal{A} \leftarrow \{\rho', \delta' \in \text{rotevts} : r_1 \leq \delta' \leq r_2\}$ 
     $\theta \leftarrow \max_{\rho', \delta' \in \mathcal{A}} \rho' - \min_{\rho', \delta' \in \mathcal{A}} \rho'$ 
    if  $\theta > \pi$  :
         $\theta \leftarrow \max_{\rho', \delta' \in \mathcal{A}} (\rho' + \pi \bmod 2\pi) - \min_{\rho', \delta' \in \mathcal{A}} (\rho' + \pi \bmod 2\pi)$ 
    return  $\mathcal{A}, \theta$ 

```

Table 2: A *pseudo-code* implementation of the *fullAnnuli* routine in mathematical shorthand.

These two pieces of *pseudo-code*, programmed in Python, provide the ability to make precise event regions of multiple radial distances simultaneously. Partial annuli are particularly useful for directional analysis, or for selecting very narrow regions for analysis without the use of masking files. The full annuli code is particularly useful in central cluster observations, where the creation of single complete annulus is possible. An annulus defining system is necessary for the use of cluster mass mixing models.

The rotating algorithm may be described as follows: Let ρ_0, δ_0 be the right ascension and declination, respectively, of the center observation. The position of these coordinates on the unit sphere is the vector $z' \equiv \langle \cos \rho_0 \cos \delta_0, \sin \rho_0 \cos \delta_0, \sin \delta_0 \rangle$. As we want this coordinate to be rotated to the north pole of the unit sphere, it is desired to rotate the point around

a pivot on the equator of the unit sphere. The coordinates of this pivot point are $\rho_0 + \pi/2$ right ascension, 0 declination. The vector coordinates on the unit sphere of the pivot point are $y' \equiv \langle -\sin \rho_0, \cos \rho_0, 0 \rangle$. The crossproduct is given by:

$$\begin{aligned} x' &\equiv z' \times y' \\ &\equiv \langle -\cos \rho_0 \sin \delta_0, -\sin \rho_0 \sin \delta_0, \cos \delta_0 \rangle \end{aligned}$$

Together x' , y' and z' form a 3 dimensional rotation matrix R

$$\begin{aligned} R &= \begin{pmatrix} x' \\ y' \\ z' \end{pmatrix} \\ &= \begin{pmatrix} -\cos \rho_0 \sin \delta_0 & -\sin \rho_0 \sin \delta_0 & \cos \delta_0 \\ -\sin \rho_0 & \cos \rho_0 & 0 \\ \cos \rho_0 \cos \delta_0 & \sin \rho_0 \cos \delta_0 & \sin \delta_0 \end{pmatrix} \end{aligned}$$

The action of this matrix rotates ρ_0, δ_0 to the z axis and $\rho_0 + \pi/2, 0$ to the y axis. To rotate a particular event with coordinates ρ, δ , and corresponding unit vector \hat{v} , the dot product R :

$$R \cdot \hat{v} = \begin{pmatrix} \sin \delta \cos \delta_0 - \sin \delta_0 \cos \delta \cos (\rho - \rho_0) \\ \cos \delta \sin (\rho - \rho_0) \\ \cos \delta \cos \delta_0 \cos (\rho - \rho_0) + \sin \delta \sin \delta_0 \end{pmatrix}$$

It can be seen that ρ' , the rotated right ascension of the event being rotated up to the north pole is given by:

$$\rho' = \arctan \left(\frac{\cos \delta \sin (\rho - \rho_0)}{\sin \delta \cos \delta_0 - \sin \delta_0 \cos \delta \cos (\rho - \rho_0)} \right)$$

In the interest of computing annuli sections, it is necessary to compute the great circle distance of ρ, δ from ρ_0, δ_0 . This is given by the *Vincenty great circle distance formula* [15] which is associated with the new declination of the rotated event:

$$\delta' = \arctan \left(\frac{\sqrt{(\cos \delta_0 \sin (\rho - \rho_0))^2 + (\cos \delta \sin \delta_0 - \sin \delta \cos \delta_0 \cos (\rho - \rho_0))^2}}{\sin \delta \sin \delta_0 + \cos \delta \cos \delta_0 \cos (\rho - \rho_0)} \right)$$

Since both ρ' and δ' have many terms in common, they can be computed together efficient.

The resulting algorithm is implemented in the `rot` function in the `filter_annuli.py` module. It is describe below using *pseudo-code* in Table 3.

2.4 Objective and Background Spectra Generation

Spectra were generated using the ESAS mos-spectra task. CCDs to be excluded were automatically loaded as described in §2.2. Instrument and exposure number were also automatically generated from processed data. For all observations of Perseus, images were

```

rot( $\rho_0, \delta_0, \rho, \delta$ ):
     $\rho' \leftarrow \arctan\left(\frac{\cos \delta \sin(\rho - \rho_0)}{\sin \delta \cos \delta_0 - \sin \delta_0 \cos \delta \cos(\rho - \rho_0)}\right)$ 
     $\delta' \leftarrow \arctan\left(\frac{\sqrt{(\cos \delta_0 \sin(\rho - \rho_0))^2 + (\cos \delta \sin \delta_0 - \sin \delta \cos \delta_0 \cos(\rho - \rho_0))^2}}{\sin \delta \sin \delta_0 + \cos \delta \cos \delta_0 \cos(\rho - \rho_0)}\right)$ 
    return  $\rho', \delta'$ 

```

Table 3: A *pseudo-code* implementation of the `rot` Python function

generated along with the spectra for the energy ranges of 400 eV through 1.2 keV and 2.0 keV through 7.2 keV. Such image generation is optional and time intensive, but for the purposes of this paper, image generation was necessary to provide redundancy and confirmation than correctly formatted annuli sections were generated. The `mos-spectra` task uses the now rotated and redefined event files to produce the annular-shaped spectral regions as well as necessary intermediate files for the second task, `mos-back`, which generates the model particle background spectra.

Ancillary response files (ARF) and response matrix files (RMF) are also created for each spectra generated. The ARF files provide the ability to use the spectra generated in any standard high-energy spectra analysis software by calculating the effective area of the detector in question, while the RMF similarly follows preset standard conventions to describe the actual behavior of the detector as a function of energy, through the use of the calibration files (§2.1).

Object spectra, background spectra, ARF, and RMF files are grouped together as one main spectra file through the use of the `grppha` program. This permits the quick and easy loading of all the necessary spectral files into whichever analysis program is to be used, simply by specifying the grouped spectra file.

2.5 Automation Framework

The tasks listed in the previous sections consume a large portion of time and computer power to properly generate. However, the process itself can run into errors in various places. The use of the GNU `make` automation program was indispensable. It permitted this investigator to create a single recipe outlining each step that needed to be taken before the next task in the pipeline should be run. At the end of each task, a file would be generated should no fatal errors occur. The existence of these "completion files" were listed as dependencies on the next set of processing tasks. If the file wasn't created, the program would halt analysis at the point of failure. This permitted extensive debugging procedures that previously weren't available, as well as greatly reducing user error while compiling the parameters necessary for each task. This modular design is extremely portable and can be run on nearly any UNIX-based computer, greatly simplifying the ESAS procedure. One major benefit of this system is the capability to do batch processing for numerous spectra at once, which reduced processing time significantly.

2.6 Spectra Analysis

2.6.1 Spectra Preparation

Spectra were analyzed using the 12.7.0 release of the **XSPEC** spectral analysis software package. Local **NFWMASS** and **CLMASS** models were used for the purposes of this analysis. Cosmological constants in use were $H_0 = 70$, $\Omega_\Lambda = 0.73$, $\Omega_m = 0.27$, and relative solar abundance used for all abundance fitting parameters. Systematic error was fixed at 0.

Spectra were loaded in groups of three or four as defined by the observation the spectra originated from. The spectra analyzed were derived from the full annulus mode of the spectra generation tasks (§2.4), but were grouped by observation to preserve directionality.

Bad event responses were ignored immediately. Any events below the range of .6 keV and above 8.0 keV were excluded from fitting, due to the falloff at higher energies and the non-standard response of the MOS detectors below ~ 0.4 keV.

2.6.2 Fitting Procedures

Fits were run using the standard statistical package loaded into **XSPEC**; χ^2 statistics were used for the fitting.

All fits were done after first varying to parameter to be fit until the resultant χ^2 value was reasonably decreased from the default parameter value. In cases where background parameters were fit, the program was left to attempt a fit without any adjustment initially, due to the large number of parameters needed to be varied simultaneously to achieve a good fit (~ 40 parameters).

2.6.3 Soft Proton, Cosmic Background, and Instrumental effects

As described in the ESAS Cookbook [14], the background was modeled by multiple components for local foreground, instrumentation, and cosmic background sources. Gaussian model components were used to describe the two radiation sources (Al K- α and Si K- α), with energies of roughly 1.49 and 1.75 keV. For each spectra, a power-law model was added with a photon index fixed at 0.2 across all spectra, as recommended. These power-law components were not folded into the instrument effective area, depending only upon the RMF file of each spectra.

Cosmic background was modeled through the use of ROSAT All-Sky Survey archival data. An annulus of the region between 1 and 1.5 degrees from the center of the cluster was added to the loaded spectra and fit directly for the first four channels of the detector [14]. This provided the necessary low energy cosmic background filtering. The models applied to this spectra included a low energy ($< .1$ keV) thermal **APEC** component (unabsorbed), an absorbed thermal **APEC** component of a slightly higher energy ($\sim .25$ keV), and an absorbed power law fixed at a photon index of 1.46 to account for background cosmological X-Ray sources (normalization fixed to the canonical value 8.88×10^7). Once the background model parameters were well fit, the RASS spectrum itself was excluded, as the spectra used interfered with the fitting of the mixing models used in the mass analysis.

Two Gaussian components, centered at 0.65 keV and 0.56 keV were also included to account for solar wind-ionized particle contamination, but almost universally these models

return extremely low, non-fitting normalizations and were locked at zero intensity.

2.6.4 APEC and VAPEC Cluster Emission fitting

Once the background had been well fit, an absorbed thermal APEC component was loaded as the primary model for all source spectra. Redshift for these APEC components was fixed at the standard value for Perseus of 0.0183 [12, 6]. Abundances and temperatures for each spectra were allowed to vary freely. The absorbed component was set to values derived from the X-Ray Background Tool used to generate the ROSAT background spectrum.

Once the standard APEC model was reasonably well fit, with a reduced χ^2 of ~ 1 , it was replaced with a VAPEC model. A VAPEC model allows more precise control of the abundances of 12 different elements. For the purpose of this study, all alpha elements [7] were linked to the abundance of oxygen, which was allowed to vary, while Fe was allowed to vary freely. All other elemental abundance parameters in the VAPEC model were frozen at zero. Similar to the APEC model, all normalizations were frozen to the innermost annuli spectra.

APEC models were chosen due to the ability to select one central abundance as well as the ability to switch between the standard model and the variable abundance model with ease. Further, the APEC model is based upon the principle that the source emission, which is an ionized plasma contained in the ICM of Perseus, was ionized through collision processes. Such a model, based upon thermal bremsstrahlung and line emission processes, is a reasonable emission model for the Perseus cluster [2].

2.6.5 Mixing Model Fitting

Following the fitting of the APEC and VAPEC models, the models were further edited to include the mixing models NFWMASS [9] and the CLMASS model.

NFWMASS was initially fit as a simple test to confirm the spectra were properly formatted. In one case, the spectra had some slight overlap between annuli sections, resulting in errors. This spectra was excluded from all analysis. To provide a good fit for the mass density $\rho_0/(r/a(1 + r/a)^2)$ and total mass of the region M_{total} (Equations (2) and (3)), temperatures were linked to the proper temperature components of the model, while the scale length a and potential U were varied manually initially to roughly expected values, to ensure that the fitting procedure would converge. The thermal models were absorbed APEC models (§2.6.4), as opposed to VAPEC models, so as to reduce the uncertainty of the large number of parameters in the VAPEC model.

$$U = 4\pi G \rho_0 a^2 \mu m_H \quad (2)$$

$$M_{total} = \int \frac{4\pi r^2 \rho_0 dr}{r/a(1 + r/a)^2} \quad (3)$$

Once NFWMASS models were well fit, the NFWMASS component was exchanged for a CLMASS component, for the derivation of electron number density and gas densities. Similar temperature linking procedures were utilized, while densities for each shell were allowed to vary freely after being set to roughly expected values [13]. Densities for each region were produced in the units of (4):

$$\rho = \frac{keV}{G\mu m_H u^2} \quad (4)$$

where u is in units of arcseconds. Conversions to cgs units can be found in §3.2.

In each case, beta models were not used, as the outer annulus was taken to be the approximately outer emission from the cluster. Normalizations for each spectra were tied to the normalization of the innermost annuli, as this normalization describes the flux through all of the shells of the spherical cluster. The inner radial distance from the center of the cluster were in units of arcseconds. To describe the angular extent of each region the **AREASCAL** keyword within the spectra file was edited to the appropriate value for each spectra, while the outer edge radial distance of each annuli was stored in the **XFLT001** keyword, as specified [10].

3 Results

3.1 Tabulating Results

From Table 5, it can be seen that much of the analysis was plagued by high levels of uncertainty in the parameter fit, despite generally acceptable χ^2 statistics. In the case of the VAPEC model (Table 4), this was generally not a significant issue, though it was apparent that the linking of so many alpha elements together added an unnecessary level of uncertainty into that parameter. Iron abundances tended to be reasonably well fit by comparison, with significantly lower uncertainties in almost all regions. CLMASS and NFWMASS model fits experience high levels of error (Table 5). In comparing density, gas fraction, and baryon fraction results with Simionescu et al. and Sanders et al., it is apparent that the results obtained were generally within a factor of ten of the previous studies' reported results (see §3.2).

RA	DEC	R_1	R_2	Temperature (keV)	α	Error (+/-)	Fe
49.927795	41.234965	800	1200	5.26472	0.189976	0.139367	0.229348
49.950017	41.12178	1200	1600	5.29385	0.121239	0.100111	0.170956
49.948232	41.014835	1600	2000	4.97118	4.92575×10^{-5}	0.139413	0.12039
49.970342	40.912062	2000	2400	4.21623	0.332269	0.312645	0.240518
49.929748	41.779298	800	1200	6.53401	0.173715	0.199214	0.140577
49.931043	41.89284	1200	1600	6.89425	5.84522E-08	NO FIT	0.245601
50.014582	42.002226	1600	2000	5.15523	6.53775E-08	NO FIT	0.148863
49.956595	42.098751	2000	2400	2.71061	1.89836	1.25537	0.0764963

Table 4: Sample of VAPEC model temperature, α and Fe abundance fit from ObsID 0085590201.

3.2 Calculation

To generate the final density and mass numbers the annular regions, from the provided numbers generated by the NFWMASS and CLMASS models, a few calculations had to be made to first. Angular and luminosity distances were calculated to provide a value of roughly .367

RA	DEC	R_1	R_2	a	Error	U	Error	ρ_0	Error
49.927795	41.234965	800	1200	104.222	444.886	69.3545	147.579	1.58×10^{-6}	4.81×10^{-7}
49.950017	41.12178	1200	1600	104.222	444.886	69.3545	147.579	9.79×10^{-7}	5.21×10^{-7}
49.948232	41.014835	1600	2000	104.222	444.886	69.3545	147.579	NULL	NO FIT
49.970342	40.912062	2000	2400	104.222	444.886	69.3545	147.579	1.36×10^{-10}	1.86×10^{-6}
49.929748	41.779298	800	1200	186.405	1215.18	95.7897	266.187	2.65×10^{-6}	4.32×10^{-6}
49.931043	41.89284	1200	1600	186.405	1215.18	95.7897	266.187	9.58×10^{-7}	6.19×10^{-6}
50.014582	42.002226	1600	2000	186.405	1215.18	95.7897	266.187	9.04×10^{-8}	8.44×10^{-6}
49.956595	42.098751	2000	2400	186.405	1215.18	95.7897	266.187	7.47×10^{-6}	8.44×10^{-6}

Table 5: **NFWMASS** fit for a and U and **CLMASS** fit for ρ_0 from ObsID 0085590201 and ObsID 0305690301 respectively. a and U are the same for all annuli of each observation, as only one value is provided for each spectral group.

kpc/arcsec and 3×10^{21} meters [17]. This conversion factor was used both in the calculation of the gravitating mass density derived from **CLMASS** as well as gravitational potential from **NFWMASS**. A constant factor of 1.6×10^{-9} in units of ergs/keV was included. The value of 0.62 is used for the mean mass fraction of a full ionized plasma [1], while 1.6×10^{-24} grams is used as the mass of a proton.

The gas density from **CLMASS**, in cgs units of grams/cm³, is given by the equation:

$$\rho_g = \frac{1.6 \times 10^{-9} \cdot \rho_0}{G(.6 \cdot 1.6 \times 10^{-24}) \cdot (.367 \cdot 3 \times 10^{21})^2}$$

The electron number density is given by the equation:

$$n_e \equiv N_e/V = \frac{\rho_g}{1.6 \times 10^{-24}} \times \left(1 - \frac{m_e \cdot N_e}{m_H \cdot N_H}\right) \cdot \frac{N_e}{N_H} \approx \frac{\rho_g}{1.6 \times 10^{-24}}$$

While the total mass density of the region is provided (via **NFWMASS**):

$$\rho_t = \frac{1.6 \times 10^{-9} \cdot U}{G(.6 \cdot 1.6 \times 10^{-24}) \cdot (a \cdot .367 \cdot 3 \times 10^{21})^2}$$

Finally, the baryon fraction is provided by:

$$f_{gas} \equiv \frac{\rho_g}{(\rho_t - \rho_g)}$$

In comparison to previous studies of the Perseus cluster, notably the aforementioned study by Simionescu and a related study by Sanders et al. [13, 12], it has been determined that the error from the anticipated results were roughly of an order of magnitude higher, in the case of gas mass density, and an order of magnitude too low for the gas fraction (Fig. 5). However, due to the expectations of the sources of error and the extent to which these errors could alter these results, these error margins are considered to be acceptable. More rigorous practices must be utilized in future study of this region.

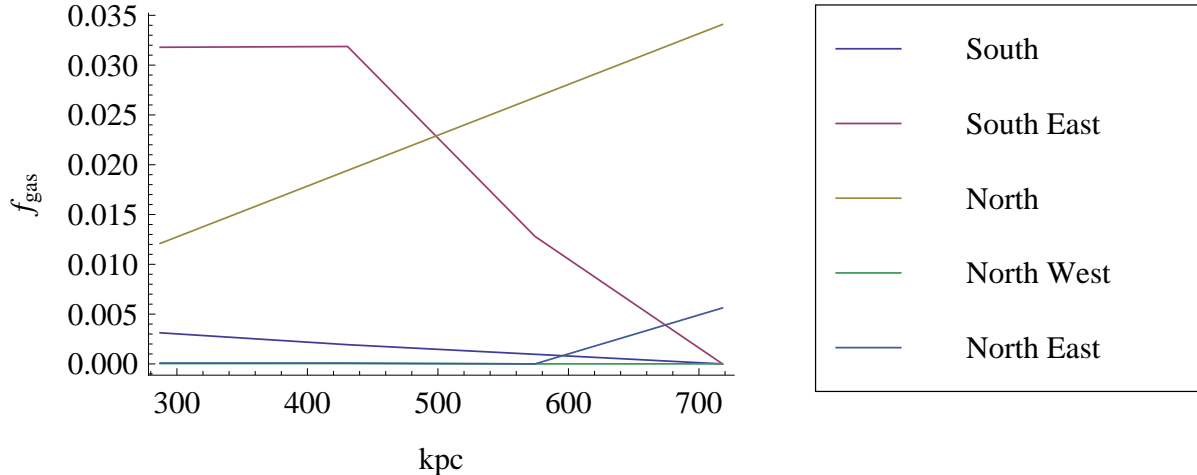


Figure 5: The dependence of the deprojected f_{gas} , the baryon gas fraction, as a function of radius. High levels of error skew this results an order of magnitude too low.

In the case of temperature profiling and iron abundance, via the **VAPEC** model, results were far closer to presently accepted values to within a respectable margin of error [2]. However, it is desirable to produce higher quality results for across the entire region, as the size of the annular sections used in this study are of significant breadth compared to the whole of the observed clustered. This provides a major limitation on the ability to pinpoint exact regions and define temperatures, as the temperatures and elemental abundances produced by the **VAPEC** model are not provided as a direct function of radius. Increasing the number of annular regions, as mentioned in §4, is expected to provide a continuous function describing the temperature and abundances dependent on direction and radius as well as significantly improved statistics. One significant area of concern, as mentioned below in 3.3, is the distinctly non-uniform temperature distribution of the cluster (Fig. 6). This, tied with the spread of abundances observed (Fig. 7), provides reason to argue that the Perseus cluster does not model a system in hydrostatic equilibrium [6, 5]. However, it is expect that further study (§4) should yield results with more reasonable error to combat this potential failing of the mass mixing models.

As described in [12], non-spherically symmetric bubbles and ripples in the immediate central region of the cluster exist, while in some cases shock waves extending out to ~ 170 kpc. This could particularly be indicative of recent interactions and collisions with galaxies or the infall of large quantities of matter into the central AGN. Furthermore, there is recent evidence of significant gas motion within the immediate 100 kpc of the central AGN [4]. With these considerations, it is possible that some error in the model fitting stems from the failure of the initial assumption concerning the equation of state of the cluster itself.

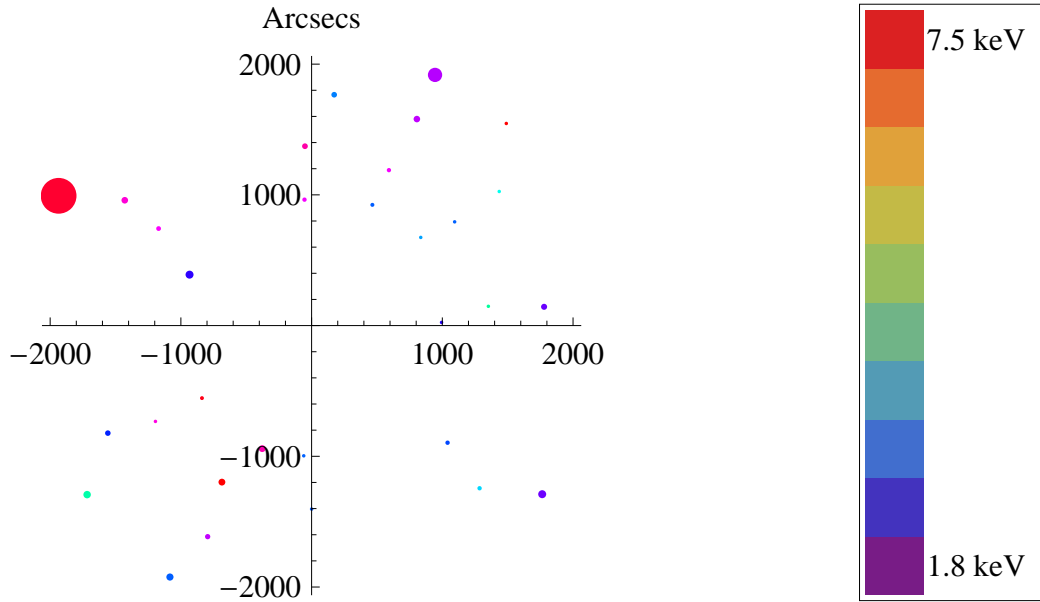


Figure 6: A profile of the projected temperatures across the Perseus cluster. Circle size is indicative of the level of error of the parameter value. Cluster center is at the origin. The code referenced in §2.3.1 was used to provide the coordinate rotation to produce both Fig. 6 as well as Fig. 7. North is in the direction of the upper left quadrant.

3.3 Error Considerations

While the error observed in this study was seen to be unusually high, much of the error, it is believed, can be reduced in future analysis. Only one detector was used in this analysis, though spectra were produced for both the MOS1 and MOS2 detectors initially. This current work on the MOS1 detector was done simply as a test case to ensure that results obtained from this new method were not significantly different, to the point where this method of analysis should be abandoned. The elimination of the second detector poses unique problems. Statistics were greatly reduced by only using half of the data, averaging results across the two detectors was not an option, and the inadequate performance of the primary detector due to physical damage.

The detector used in this study was damaged in a micrometeorite impact, resulting in the total loss of the CCD6 of the MOS1 detector. In normal operation, such a loss would not be of significant detrimental effect to the quality of observation data; annular sections could be lacking significant amounts of the effect light collecting area (Fig 9). This is obvious when the statistical robustness of the Fe abundance and temperature fitting from the VAPEC models is considered, as this model doesn't rely upon the annular shape for fitting. Large gaps in the annular sections are expected to have been a major source of error for the CLMASS and NFWMASS models, as mixing models are dependent upon having a continuous set of annuli from a defined inner radius to the edge of the cluster (or to the farthest radial extend possible).

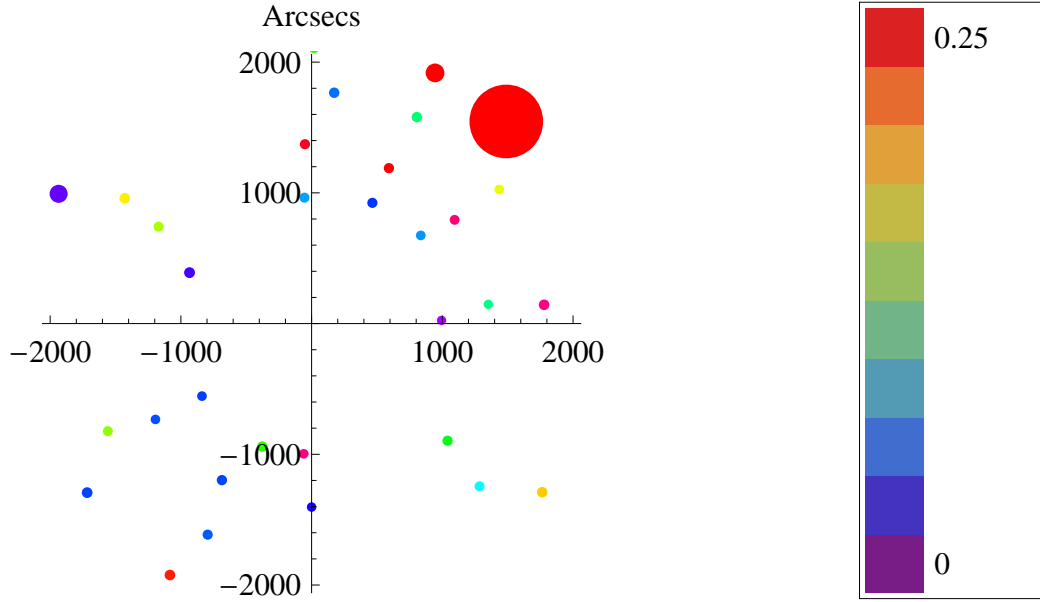


Figure 7: A profile of the Fe abundance across the Perseus cluster. Circle size is indicative of the level of error of the parameter value.

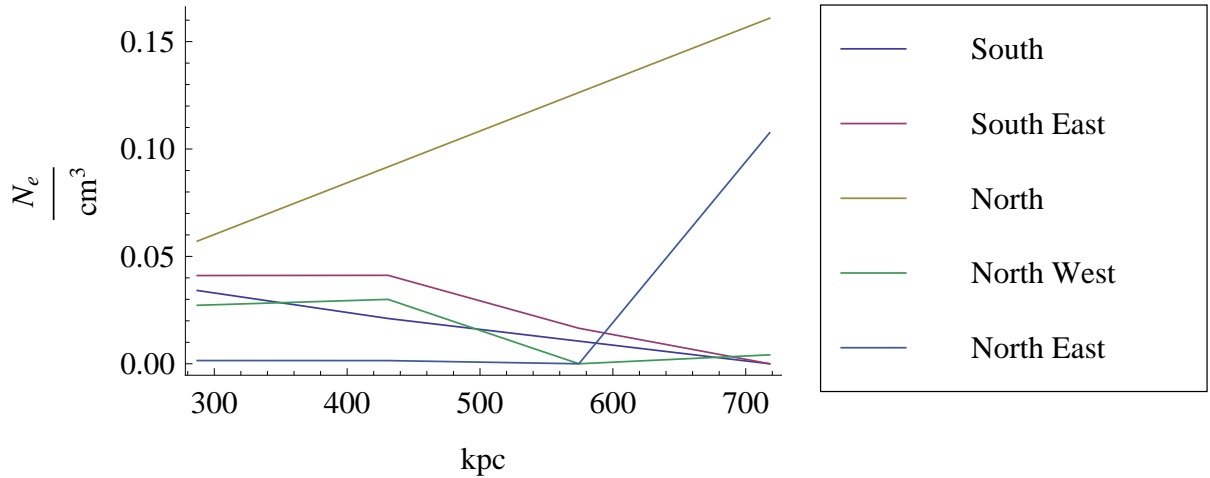


Figure 8: A profile of the electron number density across the Perseus cluster. In combination with Fig. 6 and Fig. 7 are the main examples of high error stemming from the NFWMASS and CLMASS model fits.

Another potential source of induced error was the chosen spacing and angular size of the annular regions. For the purpose of producing spectra that would be guaranteed to have adequate numbers of events, large regions, some annuli sections with $> 30,000$ events were used. The parameters for the annular sections were set to have radial extent of $400''$, while



Figure 9: On left: Image from the annuli across $1200''$ through $1600''$ with damaged CCD region in upper right corner. On right: Image from annuli across $1200''$ through $1600''$ for the intact MOS2 detector. Exposure retrieved from ObsID 0305690301.

the angular size varied between $\frac{\pi}{6}$ to roughly 2π radians. In the course of the analysis, it was determined that having too few spectra for each directionality strongly limited the ability of the mass mixing models to general accurate fits. Simply, there werent enough data points to produce reliable statistics for the gravitational potential and mass density parameters.

4 Future Study

The pn-CCD has yet to be tested in this method, though in previous study, its ability to adequately deal with background noise was much more limited than the MOS instruments. However, in the effort to improve statistical quality of results, its use in this form of analysis will be revisited.

Using the partial annulus mode described in §2.3.1, the angular extent of the spectrum derived can be shrunk considerably, while the radial size can also be reduced to at least a factor of 4 smaller. Considering just the reduction in radial size, this would potentially produce **NFWMASS** and **CLMASS** fits with significantly reduced error, providing potentially 4 or more times the amount of data points for the mixing models to fit. It is also possible to extend farther into the core of the cluster, where the quality of the X-Ray data is significantly higher, due to both the higher incident flux from this region, as well as the existence of two separate observations of the same region. This will permit the ability to greatly improve the statistics of the model fittings for the innermost regions of the cluster.

While this study has been unable to produce results of great statistical value, it has been shown that, with some adjustments, this method of analysis could provide great insight into the composition, temperature, and matter distributions of "local" clusters. With this in

mind, it is logical that the next step is to examine other clusters with a similar methodology. Furthermore, the automated procedure outlined in this paper was designed for the purpose of wide scale application. Study of clusters such as Coma, Virgo, and Ophiucus are expected to take place in the not-too-distant future.

5 Acknowledgements

I would like to thank several mentors and colleagues who have made this research paper possible. Professor Melville Ulmer has guided me for the past two years, constantly providing insight and motivation to move forward so that I could complete this paper. Professor Ulmer provided significant moral support and stress relief owls, as well as constantly being around to check the theoretical implications of my results.

I would like to thank Matthew Wampler-Doty, for his expert assistance throughout the project. His mentorship – essentially, teaching me how to program in multiple languages over the course of six months – has been invaluable. Considerable effort and time was spent creating the backbone of the rotation matrix and spherical trigonometry, as well as advising on the creating of the automation framework. Finally, his assistance with some of the formatting and graphics for this paper was indispensable.

Paul Nulsen and Steve Snowden, creators of the CLMASS and ESAS package were both incredibly helpful throughout the process of analyzing data and writing this paper. Both made themselves available over phone and email regularly and were glad to answer any questions and concerns I had.

Thanks must also be made to the committee of the Illinois Space Grant Consortium, for the grant received during the Summer of 2011, during which a significant amount of preparation and initial testing that was integral to the completion of this thesis.

References

- [1] Clabon Walter Allen and Arthur N. Cox. *Allen’s Astrophysical Quantities*. Springer, 2000.
- [2] K. A. Arnaud, R. F. Mushotzky, H. Ezawa, Y. Fukazawa, T. Ohashi, M. W. Bautz, G. B. Crewe, K. C. Gendreau, K. Yamashita, Y. Kamata, and F. Akimoto. Temperature and iron abundance variation of the gas in the perseus cluster. *The Astrophysical Journal Letters*, 436:L67–L70, November 1994.
- [3] David Arnett. The first supernovae. *Astrophysics and Space Science*, 265(1):29–35, 1999.
- [4] E. Churazov, W. Forman, C. Jones, R. Sunyaev, and H. Bhringer. XMMNewton observations of the perseus cluster II. evidence for gas motions in the core. *Monthly Notices of the Royal Astronomical Society*, 347(1):29–35, January 2004.

- [5] A. C. Fabian, E. M. Hu, L. L. Cowie, and J. Grindlay. The distribution and morphology of x-ray-emitting gas in the core of the perseus cluster. *The Astrophysical Journal*, 248:47–54, August 1981.
- [6] A. C Fabian, J. S Sanders, S. W Allen, C. S Crawford, K. Iwasawa, R. M Johnstone, R. W Schmidt, and G. B Taylor. A deep chandra observation of the perseus cluster: shocks and ripples. *Monthly Notices of the Royal Astronomical Society*, 344(3):L43–L47, September 2003.
- [7] Francesca Matteucci and Brad K Gibson. CHEMICAL ABUNDANCES IN CLUSTERS OF GALAXIES. *arXiv:astro-ph/9503057*, March 1995.
- [8] R. F. Mushotzky and M. Loewenstein. Lack of evolution in the iron abundance in clusters of galaxies and implications for the global star formation rate at high redshift. *The Astrophysical Journal*, 481(2):L63–L66, June 1997.
- [9] Julio F Navarro, Carlos S Frenk, and Simon D. M White. A universal density profile from hierarchical clustering. *arXiv:astro-ph/9611107*, November 1996. *Astrophys.J.*490:493-508,1997.
- [10] P. E. J Nulsen, S. L Powell, and A. Vikhlinin. Model-independent x-ray mass determinations. *arXiv:1008.2393*, August 2010.
- [11] T. H Reiprich and H. Bhringer. The mass function of an x-ray flux-limited sample of galaxy clusters. *The Astrophysical Journal*, 567:716, 2002.
- [12] J. S Sanders and A. C Fabian. A deeper x-ray study of the core of the perseus galaxy cluster: the power of sound waves and the distribution of metals and cosmic rays. *arXiv:0705.2712*, May 2007.
- [13] Aurora Simionescu, Steven W Allen, Adam Mantz, Norbert Werner, Yoh Takei, R. Glenn Morris, Andrew C Fabian, Jeremy S Sanders, Paul E. J Nulsen, Matthew R George, and Gregory B Taylor. Baryons at the edge of the x-ray brightest galaxy cluster. *arXiv:1102.2429*, February 2011.
- [14] S. L. Snowden and K. D. Kuntz. Cookbook for analysis procedures for XMM-Newton EPIC MOS observations of extended objects and the diffuse background. Technical report, Tech. rep., XMM-Newton GOF, GSFC, NASA, Greenbelt, MD 20771, 2006.
- [15] T. Vincenty. Direct and inverse solutions of geodesics on the ellipsoid with application of nested equations. *Survey review*, 23(176):8893, 1975.
- [16] Matthew Wampler-Doty, Paul Geringer, Peter Maksym, and Mel Ulmer. A survey of XMM and chandra galaxy clusters in search of relativistic jets. *To Appear*, 2012.
- [17] E. L. Wright. A cosmology calculator for the world wide web. *Publications of the Astronomical Society of the Pacific*, 118:1711–1715, December 2006.